Subject-specific image analysis and computational modelling of the human Achilles tendon

Erika Thörn & Johanna Panzar

Lund, June 2021

Master's Thesis in
Biomedical Engineering

Supervisors: Thomas Notermans, Hanna Isaksson and Pernilla Eliasson

LUND
UNIVERSITY

Faculty of Engineering, LTH
Department of Biomedical Engineering

Title
Subject-specific image analysis and computational modelling of the human Achilles tendon

Authors
Erika Thörn & Johanna Panzar

Figures
The displayed figures in this report are created by the authors if nothing else is indicated

Lunds Universitet
Institutionen för biomedicinsk teknik
Box 118
SE-221 00 Lund
Sverige

E-husets tryckeri
Lund 2021

Acknowledgements

Firstly, we would like to thank our supervisors. To Thomas, for being reachable at all times and keen to help in the midst of writing your own dissertation. To Hanna, for having ideas and for your guidance throughout this project. To Pernilla, for sharing the data used in this report and for being our human Achilles tendon expert. We would also like to thank Lorenzo and Joeri for sharing your Abaqus and meshing expertise.

To the rest of the Biomechanics group and the other master's thesis students in the group, it was nice to get to hang out a few times during these pandemic times.

Abstract

Achilles tendon rupture is becoming more prevalent with an increasing population of middle aged people participating in recreational sports. A torn Achilles tendon will likely not regain its original function, and it is unknown what treatment options are optimal. The Achilles tendon structure and how the tendon heals after a rupture varies between humans. A potentially useful tool in understanding Achilles tendon healing is the use of computational models.

Data from an ongoing unpublished study (by Pernilla Eliasson) with 41 patients with ruptured Achilles tendon was made available for this project, five of these were selected for analysis. In the study, all patients did early motion training and a test group had early load training as well. The study included computer tomography (CT) images of the Achilles tendon, along with tensile loading data. The access to this patient data resulted in two aims for this project. One aim was to develop a pipeline for modelling subject-specific healing human Achilles tendons. Another aim of this project was to perform image analysis on healing human Achilles tendons from computed tomography images of these five patients, to study dimensions and tissue density throughout healing.

From CT images taken at 7, 19 and 52 weeks post rupture, the healing Achilles tendon was segmented. The free tendon length was also measured at the three time points. The segmented tendon was analysed for cross sectional area and tissue density. Segmentations of tendons were also prepared for finite element modelling. Using subject-specific experimentally measured tensile load data that had been obtained from roentgen stereophotogammic analysis (RSA), two material models were applied to the geometry, one linear elastic and one viscoelastic. The subject-specific tendon models were used for simulating tensile load and creep.

The results from the image analysis suggest that the cross sectional area and the tendon length increased within 7 weeks post rupture. The tissue density

distribution was similar throughout the tendon. The simulations predicted maximum stress and strain at the smallest cross sectional area and at the boundary conditions.

In order to get more accurate and *in vivo* like results from the simulations more experimental data is required. One year post rupture the tissue density had gone back to normal, but an increase in cross sectional area remained, suggesting that the tendon had not fully recovered. Due to the small sample size of five patients, no conclusions could be drawn about the two treatments protocols.

Acronyms and Abbreviations

ATR – Achilles Tendon Rupture

ATRS - Achilles Tendon Total Rupture Score

BP - Bursal Projection

CAT - Contralateral Achilles Tendon

CT – Computed Tomography

FE - Finite Element

HAT - Healing Achilles Tendon

HU – Hounsfield Units

RSA - Roentgen Stereophotogammic Analysis

Contents

Chapter 1

Introduction

The Achilles tendon is the largest tendon in the body [10], and Achilles tendon rupture (ATR) is one of the most common tendon injuries [36]. The incidence of acute tendon rupture in Sweden increased between 2001 and 2012 by around 20% in both men and women [14]. A possible explanation for this is increased activity in the middle aged and elderly population [14]. Another explanation is the increase of metabolic and other chronic diseases that have been connected to ATR in some reports [14]. The majority of Achilles tendon rupture indices occurs in men, as they were recorded to have 79% of the ATR cases in Sweden between 2001 and 2012. In 2012, the recorded incidence of acute ATR was 35 per 100,000 persons, for men in particular the number was 55 per 100,000 [14]. A tendon rupture will affect the quality of life. While there is a monetary cost of treating an ATR, there is also a substantial risk of the ruptured tendon not fully returning to its function prior to injury [35].

It is not known what the optimal treatment to tendon rupture is [29]. Treatment options are surgical or non-surgical, where surgical repair have been preferable due to studies showing higher risk of re-rupture in non-surgical treatment. However, there are reports of early mobilisation and weight bearing being key to decrease incidences of re-rupture after non-surgical treatments [14]. Monitoring is an important part of evaluating the progress of tendon healing.

Today, the ability to obtain high resolution medical images when monitoring the healing post ATRs allow for computer modelling and image analysis of the tendon structure. Computed tomography (CT) images were made available of healing human Achilles tendons at 7, 19 and 52 weeks post rupture with accompanying mechanical data from an ongoing unpublished clinical study by Dr Pernilla Eliasson (Linköping University). In this study, the participating

patients had undergone non-surgical treatment with early motion training. A test group was also performing early controlled load training along with the motion exercises.

1.1 Aim

The objective was to perform image analysis to evaluate the healing development and to build and simulate finite element models of the healing tendon. One aim of this master's thesis was to develop a pipeline for subject-specific finite element (FE) models of healing human Achilles tendon post rupture, in order to study the stress and strain distribution in the Achilles tendon during the healing process. This was done with geometry from CT images and material properties based on a rat Achilles tendon model [27] which was fitted to subject-specific RSA data.

In addition, another aim was to study the CT images of the healing Achilles tendon and see if any trends could be identified regarding tendon dimensions such as length and cross sectional area, and tissue density. How are these properties changing over time as the tendon is healing? This was done through image analysis of the CT images.

Finally, an exploration of however it was possible to detect differences in healing between two patient groups by comparing tissue density over time. Is there a link between density distribution and treatment choice?

1.2 Design of study

Previous work done by Thomas Notermans was used as a starting point for this master's thesis. This included optimised material parameters for a rat Achilles tendon when subjected to tensile loading. From an ongoing clinical study of Pernilla Eliasson (Department of Biomedical and Clinical Sciences, Linköping University), CT images and RSA data were available for 41 patients at three time points post tendon rupture. An initial visual screening of the images was executed manually in order to identify the images that could be segmented, after the screening five patients remained.

The segmented images from one of the five patients were used to obtain the tendon geometry used in the finite element (FE) model. In order to adapt viscoelastic material properties to the human Achilles tendon, the Young's modulus provided in the RSA data was used to fit the stiffness parameters of

the material. Subject-specific models were then obtained for one patient and a creep test was simulated. Linear elastic models were also created for the same geometries with the Young's moduli from the RSA data, for comparison of stresses and strain distributions between the two materials.

The CT images and the segmented tendons were also used to obtain the cross sectional area and the free tendon length. An evaluation of intensity values of the healing Achilles tendon from CT was also performed.

1.3 Author's contribution

This masters thesis is comprised of two overlapping sections, one with a core at image analysis and the other focusing on FE modeling. Johanna Panzar has segmented patient specific tendon geometries, and created the corresponding FE meshes from CT images. Additionally, image processing was done by Johanna to determine dimensions and to analyse spatial distributions of the CT pixel intensities within the tendons. Erika Thörn has developed finite element models for simulating human Achilles tendon behavior using the segmented and meshed patient specific tendon geometries and experimental data. Both authors have contributed equally to this report, both writing and revising.

Chapter 2

Background

2.1 Anatomical positions

When referring to the anatomical positions and directions of the Achilles tendon throughout this report, sagittal, axial, posterior, anterior, proximal and distal are the most frequent terms used. These terms are visualised in Figure 2.1.

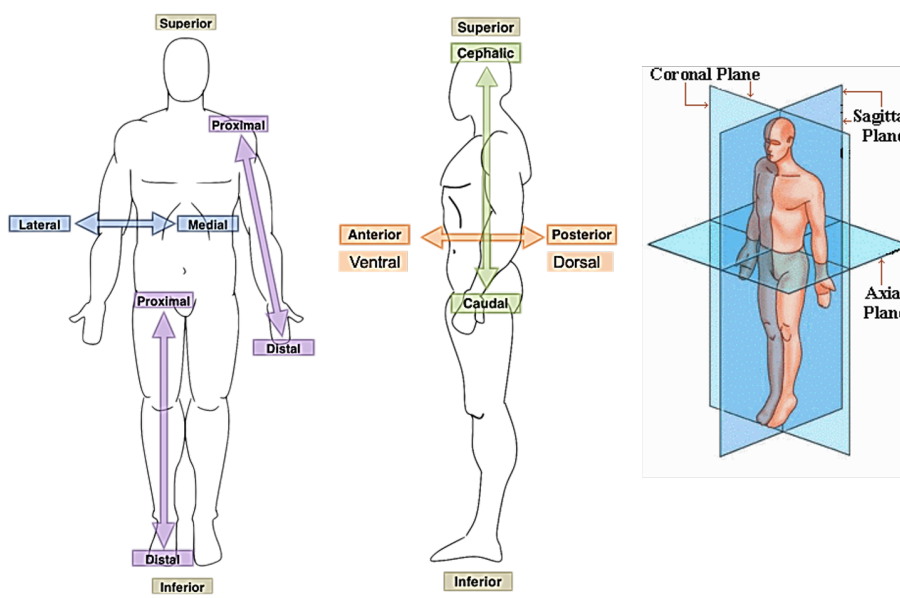

Figure 2.1: Anatomical directions and planes of the human body [21] [6].

The Achilles tendon is positioned in the lower leg, posterior (see Figure 2.1) to the tibia and fibula. The distal end is inserted to the calcaneus bone and proximally, the Achilles tendon is divided into three subtendons that are attached to the calf muscles. These muscles are known as the lateral gastrocnemius, the medial gastrocnemius and the soleus.

Figure 2.2: The anatomy of the lower leg and the position of the Achilles tendon [4].

2.2 Anatomy and pathology

2.2.1 Achilles tendon

The Achilles tendon is the largest tendon in the body and also the strongest [10] [37]. It transfers mechanical load from the gastrocnemius and soleus muscles to the calcaneal bone to allow for certain movement of the ankle joint. Proximally, it is originating from the gastrocnemius muscles in a broad flattened shape. The transition from these muscles to tendon begins at the middle of the calf. The gastrocnemius muscles are situated posteriorly in the lower leg. The soleus sits anteriorly to the gastrocnemius muscles, it is a flatly shaped muscle whose fibres transition to the Achilles tendon more distally. The gastrocnemius laterialis, gastrocnemius medialis and the soleus make up the triceps surae which allows for plantar flexion movement of the ankle via the shared Achilles tendon [10]. The muscle-tendon junction is the weakest point of the muscle-tendon unit [35]. Figure 2.3 show some landmarks of the Achilles tendon and nearby bones. The Achilles tendon insertion is at the calcaneal bone and is distributed to dissipate stresses [10].

For healthy human Achilles tendons, the tendon dimensions belonging to the dominant and the nondominant legs are similar [30]. This includes the free tendon length, measured from bursal projection to the muscle-tendon junction of soleus, and the cross sectional area of the tendon.

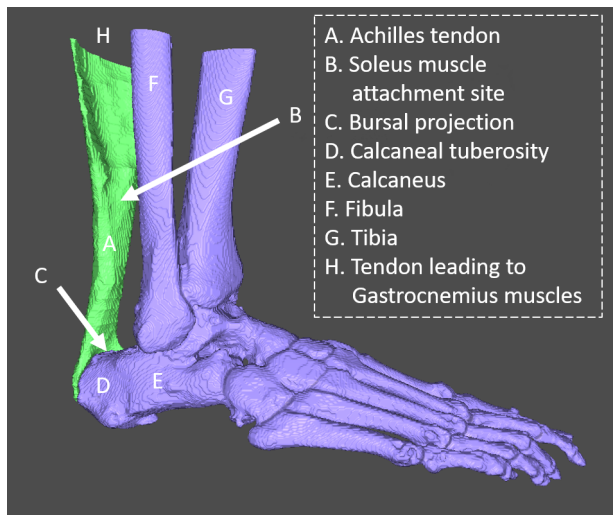

Figure 2.3: Landmarks marked on a three dimensional model of the bones of the lower leg and the Achilles tendon.

Tendon composition

The tendon tissue is composed of a collection of certain cells and extracellular matrix. The tendon tissue has low metabolic rate and low oxygen consumption, resulting in slow healing in case of injury [35]. Water is the main component of tendon tissue, responsible for 70% of total mass. The remaining 30% contains collagen type I (65-80%) along with lesser concentrations of other collagen types and proteoglycans, to name a few [40].

The tendon has a hierarchical structure, with the collagen and the non-collagenous components interwoven [40]. The collagen molecules are arranged in fibrils, sitting end-to-end. The fibrils are part of bundles known as fibres, where fibroblasts are situated along the fibrils along with a thin layer of connective tissues. The fibres, in turn are arranged in fibre bundles in several levels along with more connective tissues forming the tendon structure with parallel fibres giving the tendon its characteristic tensile strength [40]. The connective tissues contains proteoglycans, whose hydrophilic nature allows for easy transportation of water in the tissue [35].

2.2.2 Achilles tendon rupture

The tendon is a mechanically responsive tissue that change its metabolism and properties as a response to load. The tendon strength can be increased with appropriate training along with an increase in collagen type I production and cross sectional area [40]. However, overuse or misuse due to unsuitable physical training may cause tendon injury [35] [40]. Tendinopathy is an umbrella term encasing tendon injuries caused by overuse and develops over time. Acute injury of the tendon is known as tendon rupture, which occur suddenly. It has been reported that sports related ATR occurs simultaneously with an acceleration or deceleration in the musculoskeletal mechanism. There have also been reports of degenerative tendinopathy in cases of spontaneous ATR [35]. In this study, however, all patients have sustained ATR in one leg, following physical activity.

Healing process
The tendon healing after an ATR is described in three overlapping phases; inflammatory, repairing and remodeling [35] [40]. Immediately post tendon rupture, the healing process is initiated with an inflammatory response at the rupture site [35]. It then takes a few days before the repairing stage begins, with fibroblasts producing substantial amounts of collagen type III and proteoglycans at the injury site [35] [40]. The water content is high during this stage [35] [40]. The tissue formed during healing is also known as the tendon callus [2]. After about six weeks, the repairing phase merges into the remodeling stage, where the activity of cells and collagen production decreases and the tissue turns fibrous. Here, the fibres start to align along the loading direction and the synthesis of collagen type I starts to become more apparent [35] [40]. After ten weeks the final phase is initiated, which is a year long phase. The tissue turns first scar-like and, at a later stage, becomes a repaired tissue with increased bonding between collagen fibres, causing higher stiffness and tensile strength [35].

2.3 Medical imaging

2.3.1 Computed tomography

A common medical imaging modality used in clinical settings to diagnose, evaluate or create models of internal body parts of the human body is computer tomography, also known as CT. During a CT scan, collimated X-ray beams are exposed to axial planes of the body. The X-ray source is rotating

around the body in order to let the beams pass each axial plane at different angles [5]. The detector placed on the opposite side of the body to the source detects the transmitted radiation, making it possible to calculate the absorbed energy. The absorption is proportional to the density of the tissue the rays travel through, which is calibrated to form a comparable grey scale called the Hounsfield scale [5]. The Hounsfield scale goes between the values of -1000 Hounsfield units (HU) and +3000 HU, where air represents -1000 HU and becomes black in an image, water is 0 HU and the densest cortical bone shows as white and is represented by the highest HU. Fat, which is less dense than water, is represented by negative values, and soft tissues such as muscle has a higher density than water and is placed just above water on the Hounsfield scale [9]. For a reference, see Figure 2.4. The data of the CT scan can be reconstructed to form an image of each cross section.

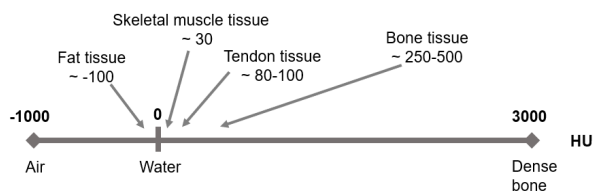

Figure 2.4: Hounsfield scale.

The distance between two image planes is the slice separation and can together with the pixels interpolate to volume pixels, also known as voxels. The slice thickness of each cross section corresponds to the collimation of the X-ray beam.

CT is an imaging modality that allows for identification of tissues with different tissue densities. For tissues with similar densities, such as muscle and tendon, the separation between the tissues is not well defined [5]. For any pixel that is placed on the interface of two such tissues, the intensity value of that pixel will be averaged. This causes a blurring of the image and makes it difficult to determine where the interface is in the image [5]. This phenomenon is known as the partial volume effect and can influence the accuracy of a tissue structure segmentation.

Another factor that effects image quality is noise and artefacts. Noise and artefacts are features in an image that appear randomised or structured, although it has no physical counterpart in the object that is imaged [17]. There can be several sources to artefacts, where some are due to the reconstruction algorithm, and they can appear differently in the images. One cause of artefact is movement, an effect that is reduced by limiting the scan time.

Another cause is metal implants, where the X-ray interfere and scatter due to the metal, resulting in streaked appearance of the cross section image [5]. Noise is usually present and will give the resulting image a degree of grainy appearance, in the worst cases it will give the entire image a spongelike texture which is difficult to remove while not removing original data. The presence of this random pattern reduces the contrast even further between low contrast tissues, making it difficult to segment these tissue structures [5].

2.3.2 Image analysis

Image enhancement

The tissue density of the Achilles tendon and the surrounding soft connective tissues are very similar in a CT image [23], and therefore must be preprocessed before performing a segmentation. One solution is to enhance the image contrast around the grey scale values of interest. By identifying the Hounsfield unit values that are present in the region of interest, the limits of the grey scale can be adjusted to highlight the tissues with pixel values between the limits. The pixel values above and below this will then be shown as white and black, respectively. Figure 2.5 show how the visualisation of the Achilles tendon changes by adjusting the contrast of a CT image.

Figure 2.5: Sagittal view of lower leg, where right image has enhanced the Achilles tendon from the surrounding soft tissue. Arrows point out metal artefacts of tantalum beads that are not visible in the current sagittal slice.

Image segmentation
The volume image of a CT scan provides a high resolution representation of the body part scanned. For further analysis of an organ or structure from the image series, a segmentation of the desired object is necessary [22]. This can be done manually, which is a time consuming method and the resulting segmentation will be user-dependent. Therefore, several automatic and semiautomatic methods have been developed over the years [22].

2.4 RSA

Roentgen stereophotogrammetric analysis (RSA) is a method commonly used when studying bone implants. When using the method to study Achilles tendons, small tantalum beads are inserted into the tendon through a needle. X-rays are then taken from two angles simultaneously, see Figure 2.6 for setup, allowing to detect the position on the beads with a 0.1 mm error in space [33].

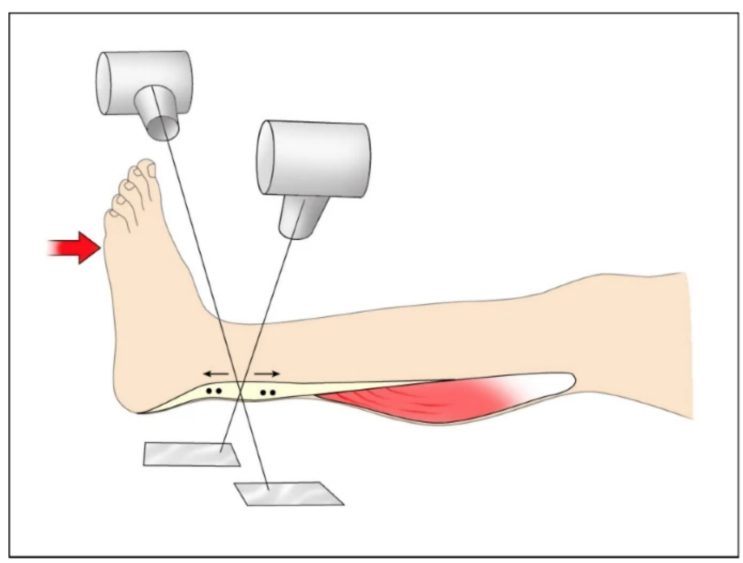

Figure 2.6: Setup for the RSA examination where the beads' position is measured during the resistance to an applied load through a pedal [33].

This method has been used to study the properties of the tendon during the healing process post rupture. The elongation of the tendon between the beads can then be observed when the tendon is subjected to a load. The test is performed by placing a pedal against the patient's foot and asking the patient to resist the load while keeping the foot in a fixed position [33]. In the ongoing clinical study by Pernilla Eliasson, the stress was estimated from the force measurements and the tendon cross sectional area, averaged between the beads. The tendon length between the beads was determined using RSA for unloaded and loaded tendon, providing strain measurement. By assuming linear elastic properties of the Achilles tendon, the Young's modulus was determined.

2.5 Biomechanics

There are two types of testing protocols that can be conducted when studying the biomechanical behaviour of a tissue, such as tendons; non-destructive and destructive testing [19]. In non-destructive testing the tissue is subjected to small loads and deformations and all changes are reversible, an example of this is creep testing. In destructive testing however, large loads are applied and the changes in the tissue are irreversible. The stress-strain curve (Figure 2.7) is often used to present results from destructive tensile testing. The initial phase of the stress-strain curve is referred to as the toe region where the stress-strain relationship is non-linear with an increasing slope for higher loads. The toe region is followed by the linear region, where the incline of this region is referred to as the Young's modulus. When remaining within these regions all changes in the tissue are reversible and the test is non-destructive. Upon reaching the yield point in a tensile test, the slope of the curve changes due to the fibrils in the tissue begin to break. This region is known as the plastic region, where the accumulation of microfractures in the collagen network ultimately leads to the point of failure [19].

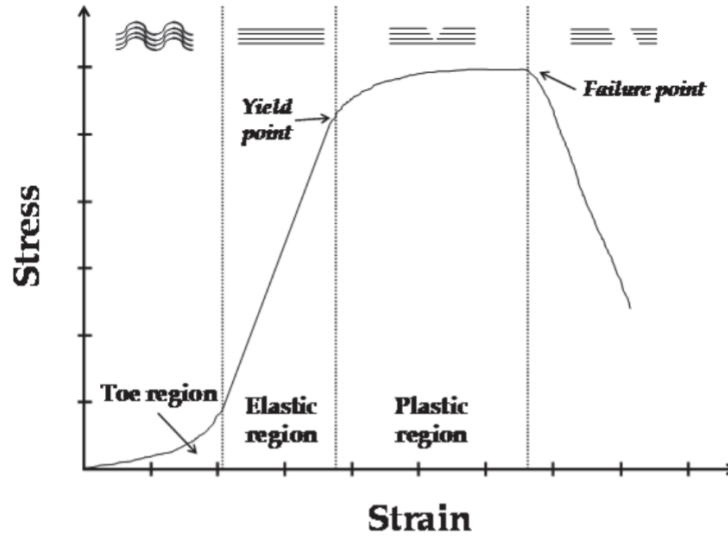

Figure 2.7: The typical stress-strain curve showing the mechanical behaviour of tendon tissue from tensile testing. Schematics of the unfolding and failure of the collagen fibrils are shown for the corresponding regions [19].

The material of the tissue can be modelled through different material models, the most simple being the linear elastic model [19]. In this model, the relation between stress and strain is assumed linear. It is a one dimensional material property but can be expanded to three dimensions when used together with the Poisson's ratio, which can express the tissue behaviour in the axial plane. One limitation of the linear elastic model is that it can not capture the time dependent behaviour of the tendon, motivating the need for a viscoelastic material model. Viscoelastic materials can be modelled through a standard linear solid model (SLS) [27] which is visualised in Figure 2.8. The two springs capture the elastic behaviour of the tendon and the dashpot captures the viscous behavior and its time dependency.

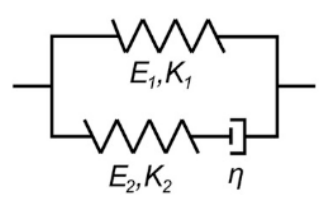

Figure 2.8: SLS used to model viscoelastic material, where E_1, K_1, E_2 and K_2 are the stiffness parameters of the two springs and η is the dampening parameter for the dashpot [27].

As the Achilles tendon mainly consists of water and collagen it is a biphasic tissue with a fluid and a solid phase, and has viscoelastic biomechanical properties. The viscoelastic behaviour can be studied in a creep test, where a load is applied and held constant for a certain time. The creep test is conducted within the linear region. Initially, the tendon experiences relaxation before it reaches an equilibrium where the strain will be constant [19].

The stress and strain that the Achilles tendon can withstand before rupture is dependent on the rate of the load. The failure stress has been determined to be around 80 MPa and the failure strain about 11 % in intact tendons [41]. While running, the Achilles tendon is subject to high forces corresponding to several times the body weight, and can experience about 6 % strain [20].

2.6 Finite element modeling of human Achilles tendon

2.6.1 Finite Element Method

Materials and mechanics are often described with differential equations, which when applied to geometries can be solved by finite element (FE) methods. The finite element method is a numerical approach for solving differential equations. This is done by dividing the geometry into many smaller parts, called finite elements. Approximations are then done for each element, instead of for the entire geometry, and to obtain the result for the whole geometry, the outcome from all elements are added together. The assembly of all finite elements is referred to as a mesh [28].

By using the FE method and assigning boundary conditions to some selected elements or regions in combination with known material properties, a more realistic model can be acquired. Examples of boundary conditions are loads and fixed node displacements [28].

2.7 Literature review

Various studies have analysed the human Achilles tendon using image analysis, mechanical testing and computational modelling. In this section, some methods and results of these studies are presented. To our knowledge there are no existing FE models of ruptured human Achilles tendons.

2.7.1 FE-modelling

The modalities that have been used in obtaining subject-specific Achilles tendon finite element models of living humans are ultrasound and MRI [8] [23]. With ultrasound, only cross section areas and shapes have been taken from the mid-section of the tendon [36] [37]. Only models of the free tendon was requested, the remaining part of the tendon was modelled by adapting a generic male model [36]. In more recent articles, 3D ultrasound has been used, capturing the whole geometry of the free tendon [13]. The conclusions drawn from the article [13] were that in healthy Achilles tendon, the stress experienced is more dependent on geometry than material properties. Using MRI, one Achilles tendon was segmented manually and went from the calcaneal insertion to the muscle-tendon junction in [12]. All models mentioned above have used a hyperelastic material model, which has the benefit of capturing the non-linearity of tendon mechanics. However, it is unable to describe the tendon as a viscoelastic material as it lacks time dependency [19].

2.7.2 Image analysis

Free Achilles tendon lengthening post ATR in surgically treated patients have been confirmed via ultrasound and MRI [11] [3]. The free tendon length has been measured in surgically treated patients, where elongation has been observed 2 weeks post surgery in patients immediately starting mobilisation and weight-bearing rehabilitation post rupture, and after 6 weeks for patients with immobilised ankles for two weeks post surgery [3].

Cross sectional area measurements have been obtained of the rupture site [3] and from averaging a few cross sectional areas of the free tendon [11] [31], but not for the entire tendon. In addition, the subjects of these studies had undergone surgical repair. In those studies, the cross sectional area was observed to increase from 6-7 weeks to 19-26 weeks post rupture, followed by a decrease to the 1 year check-up [3] [11] [31]. Tissue density calculations have been performed using CT images, by obtaining a limited number of values from circles manually placed inside the tendon callus [32].

2.7.3 Mechanical testing

Creep tests have been performed on harvested intact human Achilles tendons where the stress was ramped up to 35-75 MPa for 2.0 seconds and then held constant [42]. The maximum strains were observed just above the calcaneal insertion point, at above 20 %. The failure occured more proximal at about 2-6 cm above the calcaneal insertion where the cross sectional area was the smallest. The tendons for this study came from an elderly population, 50-70 years of age [42].

Chapter 3

Materials and methods

3.1 Materials

CT images of Achilles tendons were used in this project from a ongoing clinical trial run by Dr Pernilla Eliasson at Linköping University (Ethical permission number 2014/69-31). The patients were part of a clinical trial with a test group and a control group. The treatment for both groups were non-surgical early motion training from week 2 post rupture. The test group performed increasing load training in addition to motion training. After diagnosis, the patients had two 0.8 mm tantalum beads [33] inserted into the Achilles tendon by needle both proximally and distally in relation to the rupture. The patients were equipped with an orthosis and allowed to load the casted foot in case of no pain sensation. The test group were performing load bearing exercises from week 3 with increasing load until week 7. The exercises given to the patients are presented in Table 3.1. From week 7 onward, all patients followed the rehabilitation regime offered by the regional healthcare.

The CT images were taken of healing Achilles tendons at three time points, at 7 weeks, 19 weeks and 52 weeks post rupture. At 7 weeks, the image taken was of both ruptured and unruptured contralateral tendon. The images were obtained using a calibrated Siemens CT scanner (SOMATOM Edge Definition, slice thickness 0.75 mm, slice separation 0.3-1.13 mm, pixel size 0.28-0.61 mm, collimation width 0.75 mm).

Table 3.1: The ankle exercises were done by both patient groups, while the loading exercises were only for the patients belonging to the test group. Ankle exercises were performed three times a day, with an increased number of repetitions after 5 weeks of healing. Controlled load training was preformed by the test group two times daily with 20 repetitions at a time. From week 7 and onward, both patient groups followed the same regime designated by regional healthcare.

Week	**1-2**	**3**	**4**	**5**	**6**	**7**
Ankle exercise 3x		20	20	30	30	30
Tensile loading 2x20		30 N	75 N	125 N	175 N	225 N

There were 41 patients participating in the ongoing clinical trial. With the goal of segmenting tendons from the CT images, a visual evaluation of the images was conducted for each patient. The patients whose images at all three time points had a low noise level and sufficient resolution for manual segmentation were selected. This resulted in five patients remaining for further analysis. Out of these five, one patient was selected for developing subject-specific FE modelling, Patient 36 which had altogether good quality images for all time points.

Table 3.2 shows patient data. Highlighted in red are the two patients that are part of the test group, while the remaining three are part of the control group. All patients were doing physical exercise at the occasion of rupture, all sports related apart from Patient 36, who was cutting down trees. As part of functionality evaluation, the patients were asked to do a heel rise. The heel rise score of week 19 and 52 was measured in reference to the contralateral Achilles tendon (CAT). The last two columns include Achilles tendon Total Rupture Score (ATRS), which is a self evaluation sheet regarding function and pain from ATR [26].

Table 3.2: Patient data of the 5 patients, the two patients in the test group are highlighted in red. The heel rise score determined at 19 and 52 weeks post rupture is the HAT heel rise height (in %) in reference to the CAT heel rise height (100%). The self evaluating ATRS taken at the 19 and 52 week check-ups has a maximum score of 100.

	Sex (M/F)	Age (years)	Weight (kg)	Height (cm)	Heel rise Week 19	Heel rise Week 52	ATRS Week 19	ATRS Week 52
Patient 9	M	56	80	176	0	86	37	76
Patient 17	F	38	75	168	43	57	66	45
Patient 27	M	42	100	184	0	0	3	39
Patient 32	M	59	96	181	33	0	54	96
Patient 36	M	36	90	182	70	69	48	83

From the ongoing unpublished clinical study by Pernilla Eliasson, RSA data for the patients was available, this included calculated Young's moduli for each patient at the three time points. The applied loads used when measuring tendon lengthening are presented in Table 3.3. In the final row of Table 3.3, the range of the calculated Young's moduli of the healing Achilles tendons (HATs) for the five patients at each time point is displayed.

Table 3.3: The loading scheme used at the 7, 19 and 52 week check-ups. Each load was applied for 10-15 seconds before obtaining the RSA measurements. Between each applied load, there was a resting period of 3 minutes. The Young's modulus presented is the range for the five patients selected in this study.

	Week 7	Week 19	Week 52
Lower load (N)	0	25	25-225
Higher load (N)	100	150	225-350
Young's modulus (MPa)	22-73	66-197	87-483

3.2 Methods

3.2.1 Segmentation from CT images

The CT images were enhanced in the region of interest to increase contrast between tendon tissue and surrounding soft tissue using ImageJ [34]. The Achilles tendons were segmented manually using the software Seg3D [7]. The tendon was outlined and filled on several axial slices. In case of poor visibility,

the sagittal view was used as an aid. To limit user variability, the same person was selecting the tendon on the image slices and implementing the same selection method. Completely segmented Achilles tendons were achieved by performing morphological closing. Due to the program constraint of having a maximum radius of the spherical structuring element set to 10 slices, the distance between the manually selected slices had to be lower. From trial-and-error, the distance of 8 slices was used where the resulting segmentation had a good enough geometry and the manual workload was kept as light as possible.

The tendons segmented were of the patients presented in Table 3.2, where the healing Achilles tendon was segmented for the three time points of each patient along with the contralateral Achilles tendon imaged in the first CT scan for each patient.

3.2.2 Image analysis

Determining free tendon length
The free tendon length could manually be measured in ImageJ, using the macro 3D Distance Tool [34]. By looking at a contrasted image stack in both axial and sagittal view, the tip of the soleus muscle was found. The measurement was taken from the middle of the tendon at this axial slice to the middle of the tendon of the axial slice where the bursal projection no longer was visible.

Measuring cross sectional area
Cross sectional area of the tendon was measured in Matlab [24], where the segmentation was imported as a binary image stack. The cross sectional area was calculated at every axial slice, by counting the white pixels and multiplying with the pixel size. Due to the spherical shape of the structuring element used when obtaining the complete segmentation in Seg3D [7], smoothing was necessary. The chosen averaging filter window size was approximately 2.5 % of the number of slices, with a minimum window size of 7 slices.

Locating tantalum beads and calcaneus in CT images
The reasoning for locating the tantalum beads was twofold. Firstly, the rupture had occurred between the distal and proximal beads, indicating the volume of interest. Secondly, the tantalum beads caused metal artefacts in the CT images, disrupting the tendon intensity distribution. For plotting purposes, the calcaneal tuberosity was also located.

Using Matlab Image Processing Toolbox [25], locating the beads and calcaneus was done by using the segmentation and thresholding. By dilating each of the segmented tendon axial slices using a square structuring element that was the same size for all image stacks, the dilated version of the tendon shape was applied to the original image. Using thresholding, the axial slices containing Hounsfield units above 200 HU were located. The distal end of the tendon was determined by comparing the first and last axial slice of the segmentation, with the assumption that the part of the tendon by the calcaneus had smaller cross section area compared to the most proximal part of the segmented tendon. The top of the calcaneal tuberosity was determined as the final image slice where the calcaneus had intensity values above 200 HU in the dilated tendon shape. The lowest of the distal beads could be located after the calcaneus along with the highest of the proximal bead. To exclude the number of beads located, the proximal and distal beads were considered collections of beads, and the largest distance between the slice above the threshold was used to obtain the upper and lower limit of those groups, respectively. For the unruptured contralateral tendon segmentations, only the calcaneus was located.

Determining the tissue density and distributions

In Matlab [24], the image stack of the segmented tendon applied to the original image stack was used to calculate mean intensity and standard deviation of each axial image slice. This was then plotted in two figures, one where the mean and standard deviations of the whole tendon was presented and another where the mean values of the tendon callus between the beads was presented. When only presenting the mean intensity values, the values were filtered using an averaging filter window size of approximately 1 % of the number of slices, with a minimum window size of 3 slices. For the CAT, the bead locations of the 7 week HAT was used.

Radial sections

To get an overview of how the intensities vary with distance from the centroid within the callus, the axial segmentation was divided into three parts, see Figure 3.1. Keeping the original shape of each segmentation of the tendon slices, the three parts were obtained by eroding the shape in two turns with a disk structuring element. The size of the structuring element was calculated from using the Matlab [25] image processing function 'regionprops' and obtaining the minor axis length. To ensure three sections at all times with no overlap, the minor axis length was divided into three to get the same thickness of each section, r. The outer perimeter of the three sections are presented in Figure 3.1. The sections were generated for all slices between the beads and the mean intensities of all sections were calculated. For the intact contralateral tendon, the bead positions of the ruptured tendon at 7

weeks was used. The chosen averaging filter window size was approximately 2.5 % of the number of slices, with a minimum window size of 7 slices.

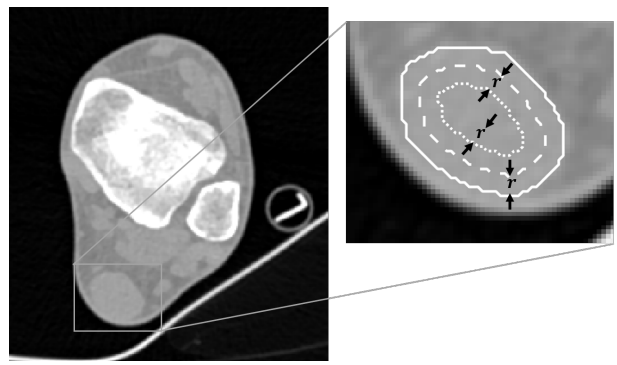

Figure 3.1: A cross section (axial) slice of the lower leg, where the Achilles tendon is outlined and the radial sections are outlined.

3.2.3 FE modeling

Mesh generation
The subject-specific geometry of the Achilles tendon was preprocessed prior to meshing. As a first step, smoothing was performed in Meshmixer [16], a program designed for preparing geometries for 3D printing. Sculpting tools and reducing mesh size were used to obtain a smooth tendon surface. The smoothed geometry could then be imported into Solidworks [39] where the tendon surface was divided into several surface sections of similar shapes to ensure simple meshing in the next step. The geometry with surfaces could then be exported as an IGES file and imported into Hypermesh [15] where an automatic surface mesh was created, using triangular elements with size 2 mm. The surface elements were adjusted so that all had inner angles of at least 20 degrees. From this mesh, a volume tetrahedral mesh was generated with 2 mm elements throughout the geometry, yielding meshes with about 30,000-40,000 elements and 6000-8000 nodes.

Meshing elements
For the linear elastic material model, the meshes consisted of C3D4 elements. These are tetrahedral elements used for volume meshes with four nodes placed in the corners, see Figure 3.2. For the viscoelastic material model, C3D4P elements were used instead. The difference between the C3D4 and the C3D4P elements is that C3D4P also handles pore pressure, which is required when modelling a biphasic material with a liquid phase.

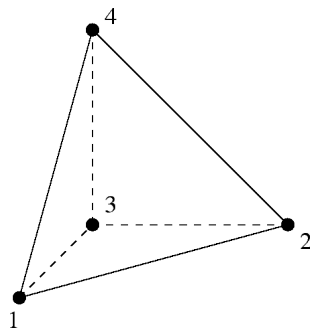

Figure 3.2: Tetrahedral four node volume element used [1].

The tetrahedral elements were chosen because they allowed better approximation of the segmented tendon geometry than brick elements which were used in previous work by Notermans *et al.* [27]. The reason for choosing four node elements was to reduce computational time.

Boundary conditions
Once the mesh had been generated it was further adapted in Abaqus/CAE 2020 [38], nodesets were assigned for the top surface, the external surface, the bottom surface as well as for the entire tendon. The top and bottom node sets were chosen according to Figure 3.3, where the bottom set represents where the Achilles tendon is attached to the calcaneus bone and the top set represents the loads from the calf muscles. The geometry was then generated in Abaqus. The main axis of the tendon was then aligned with the y-axis, this was done in Matlab [24]. This was to ensure that the fibers, defined as a part of the material in the tendon, were aligned with the y-axis and that the force was applied in the direction of the fibers.

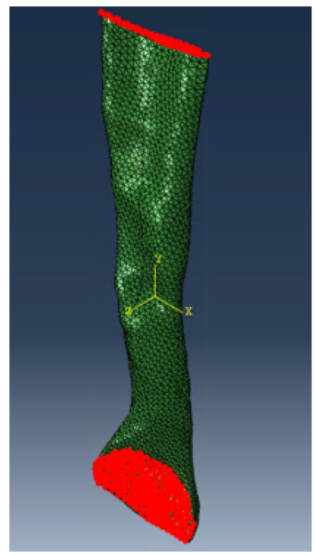

Figure 3.3: Nodesets assigned to the top and to the bottom surface.

The bottom was fixed in order to mimic the attachment of the Achilles tendon to the calcaneus bone. To make sure that the force was applied to the entire top surface, a masternode was created and placed above the top surface, the force was applied in this node. The top surface was then tied to this node using Tie Constraint, this means that the surface will have the same displacement as the masternode.

Fitting material parameters

The viscoelastic material model is based on previous work done on rat Achilles tendons, the material model was introduced by Khayyeri *et al.* and is known as a fibre-reinforced poro-visco-hyper-elastic model [18]. We implemented the material model optimised by Notermans *et al.* [27] and adapted the collagen stiffness parameters (E_1, K_1, E_2 and K_2), which are modelled by springs shown in Figure 2.8, and transversely isotropic stiffness parameters (E_p, E_n and G_{pn}) to represent the mechanical data of the RSA study. The remaining parameters from the viscoelastic material model, including the damping parameter of the SLS in Figure 2.8, were kept constant according to the optimised rat Achilles tendon model [27].

The stiffness parameters of the viscoelastic material model were fitted to the Young's modulus obtained from the RSA data. The fitting was done for each time point, through simple tensile tests. The force and displacement recorded from the simulation was normalised to stress and strain, using the

mean cross sectional area between the beads and the measured length of the tendon, and Young's modulus could be derived. The linear relationship between stresses (σ) and strains (ε) is expressed as the Young's modulus (E), $\sigma = E\varepsilon$. Young's modulus from the simulation was then compared to the Young's modulus from the RSA data. The stiffness parameters from the rat model were then manually increased with the same factor to get as close to the RSA data as possible, this was repeated until the Young's moduli differed by a maximum of 1 %.

Simulations
The simulations were performed on the HAT of one patient, Patient 36, at all three time points in order to observe how the stresses and strains were distributed throughout healing when the tendon was subjected to an applied load. Simulations of a tensile test were done both with a linear elastic material and with the viscoelastic material [27], with fitted parameters, to compare the two material models. In addition, a creep test was simulated to observe the time dependency of the viscoelastic material.

For the linear elastic models, the Young's modulus from the RSA data and the Poisson ratio was used to define the material. The Poisson ratio used was 0.3 [27]. A simple tensile test was then performed where the applied load was 350 N for all three time points. In addition, for the 7 week time point, tests with a load of 100 N were conducted. These were the loads applied via the pedal in Table 3.3 for week 52 and week 7 respectively.

For the viscoelastic material model, tensile and a creep test was performed for Patient 36 at week 7, week 19 and week 52 respectively. The material stiffness parameters were updated to the parameters acquired from the fitting to mimic the properties from RSA data for Patient 36, this was done for each time point. The load was applied in two steps, in the initial step the load was ramped up to the final load during two seconds, this is the preloading step and corresponds to a tensile test. In the second step the load was held constant for eight minutes, this time was chosen to ensure that the creep behaviour would be captured. The creep tests were run with a load of 350 N for all time points, and for the 7 week time point additional creep test with a load of 100 N was conducted as well. The load of 350 N corresponds to approximately a stress of 3 MPa for each time point and geometry.

Chapter 4

Results

In this section the results will be presented in two parts. First, the image analysis results are presented, which includes the free tendon length, cross sectional area and tissue density analysis. Secondly, the simulation results are presented, including fitted material parameters and spatial stress-strain distribution analysis from tensile loading and creep test.

4.1 Image analysis

4.1.1 Free tendon length

From manually viewing the tendon and surrounding tissue from two directions, the free tendon length could be measured, presented in Table 4.1. Assuming similar free tendon length in both lower legs of the patients prior to rupture, there has occurred elongation of the Achilles tendon from the time of rupture up to the 7-week time point for all tendons apart from Patient 36. For patients 27 and 32 there has been an additional small increase in tendon length between weeks 7 and 19. There has been no change between the rest of the time points, see Table 4.1.

Table 4.1: The measured distance between the top of the calcaneal tuberosity (BP) to the attachment site of the soleus muscle, known as the free tendon length. The patients who are tinted in grey are part of the control group, while the patients with red tint are in the test group. Measurements are in (mm).

	Week 7	Week 19	Week 52	Intact contralateral tendon at Week 7
Patient 9	88	85	85	65.6
Patient 17	90	86	89	40.4
Patient 27	109	117	119	60.9
Patient 32	73	83	83	50.4
Patient 36	57	58	57	59.6

4.1.2 Cross sectional area

The cross sectional area of the segmented tendon was calculated for the entire length of the segmentation and presented in Figure 4.1. For all 7 week plots of the HAT except for Patient 32's, there is a local minima in cross sectional area that is located between the beads, indicating the location of rupture. For all patients at the 19 week time point, tendon callus cross sectional area increased compared to the 7 week time point. Between 19 and 52 weeks, the tendon cross sectional area decreased. The cross sectional area of the entire segmented tendon post ATR is increased for all time points, assuming the cross sectional area of the healing tendon was similar to the contralateral tendon prior rupture. Generally, the location of the beads has not changed for any of the patients, see Figure 4.1.

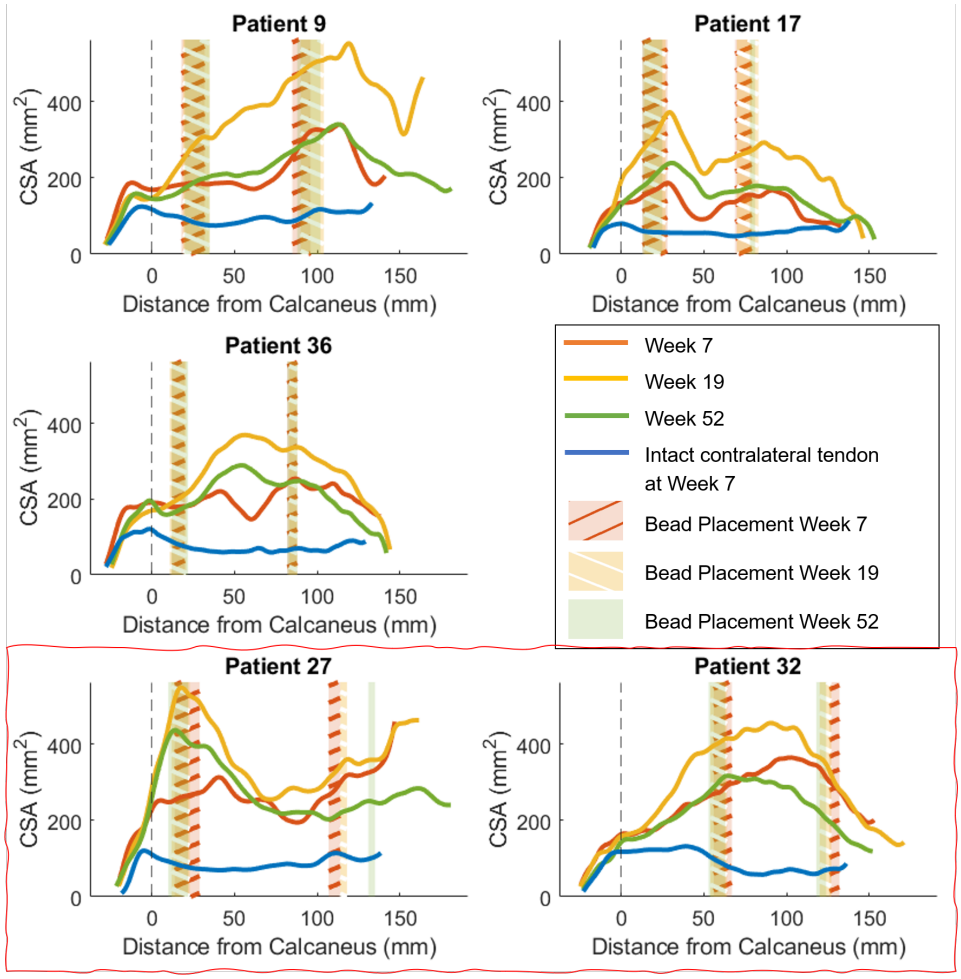

Figure 4.1: The cross sectional area of the segmented healing tendons at all time points and the intact contralateral tendon. The position of the top of the calcaneal tuberosity is marked as zero, and the beads locations along the tendon are marked in the plots. The vertical location of the beads and the placement of the calcaneus at zero indicates the height of the rupture point. The results of the patients that are part of the test group are encircled.

At the level of the distal beads in the healing tendon of Patient 27, there is also a bone-like formation. This mineralisation was present at the 7 week scan and did not show any growth until after the 19 week scan, see Table 4.2. Figure 4.2 shows the sagittal image of the lower leg at 19 weeks, with the distal tantalum beads and the mineralisation segmented.

Table 4.2: A concave disk-shaped mineralisation found distally in the healing Achilles tendon of Patient 27.

	Week 7	**Week 19**	**Week 52**
Volume (mm^3)	215	211	394

Figure 4.2: Sagittal view of the lower leg at the 19 week CT scan of Patient 27. The image has enhanced contrast. The mineralisation and the distal tantalum beads are segmented and are situated in the Achilles tendon.

4.1.3 Mean axial intensities

The mean intensity and the standard deviation of the entire segmented tendon is presented in Figure 4.3, where it has been calculated per cross section. The mean values are overall stationary along the entire tendon. There are sudden and sharp fluctuations in mean and standard deviation at the locations of the beads. For several measurements there is a lowering of mean intensity values by the calcaneal insertion along with an increase in standard deviation displayed in Figure 4.3.

A closer look on the mean intensity values found in the axial slices between the implanted beads inside the tendon are presented in Figure 4.4. In this figure, it clearly shows that *the mean intensities of the cross sections increases with each consecutive time point.* The mean intensity values of the HAT at the 52 week time point is similar to the CAT for all patients apart from Patient 32.

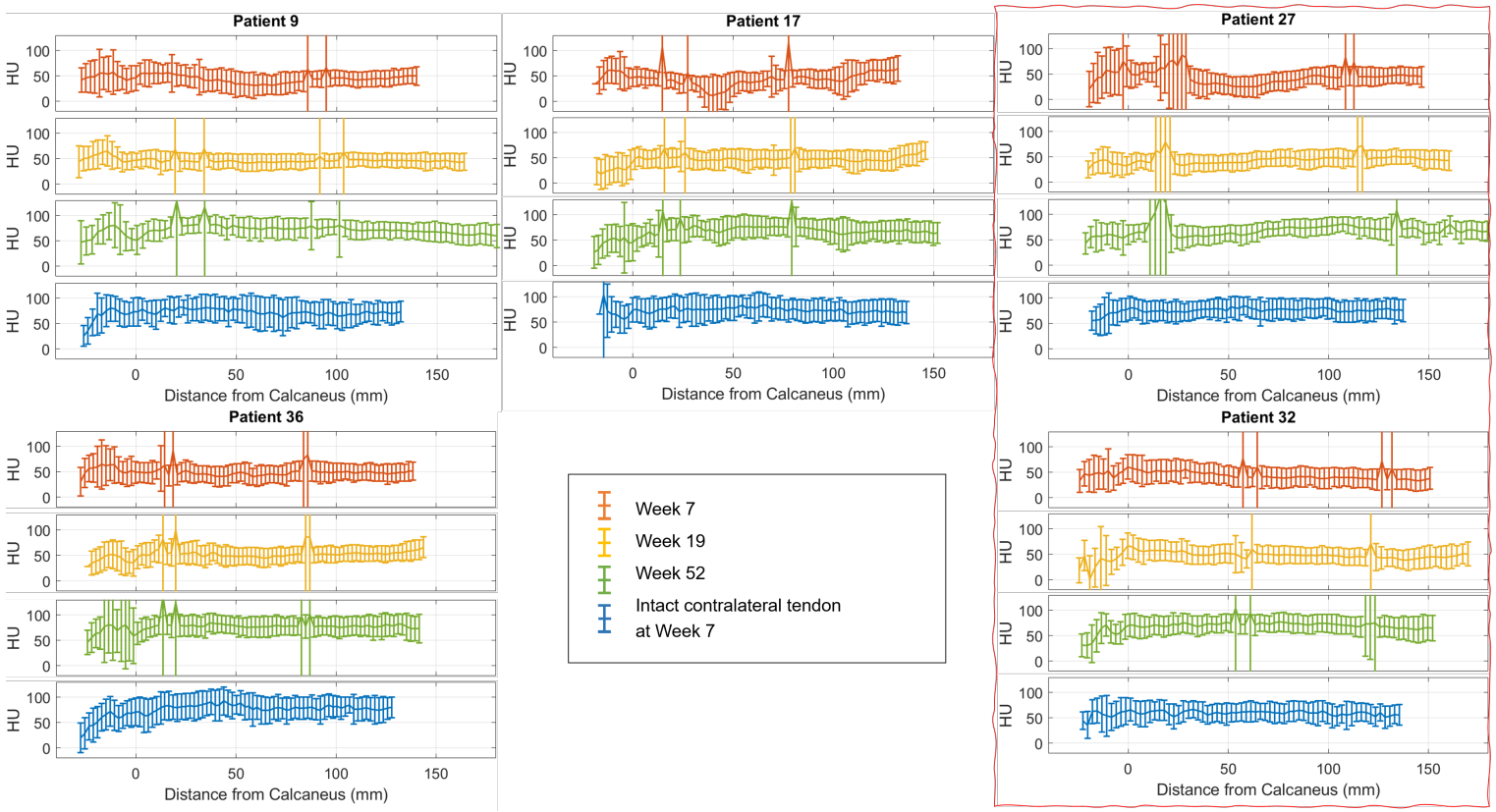

Figure 4.3: Tissue density measured in Hounsfield units of segmented tendons from CT images taken at 7, 19 and 52 weeks post rupture. The top of the automatically located calcaneal bone was defined as zero in the plots, meaning the tendon attached to the calcaneus has a negative distance to the BP. The vertical location of the tantalum beads in the HAT are identified as the instances where the mean intensity values increase, and the standard deviation is much larger than nearby cross sections. The results of the patients that are part of the test group are encircled.

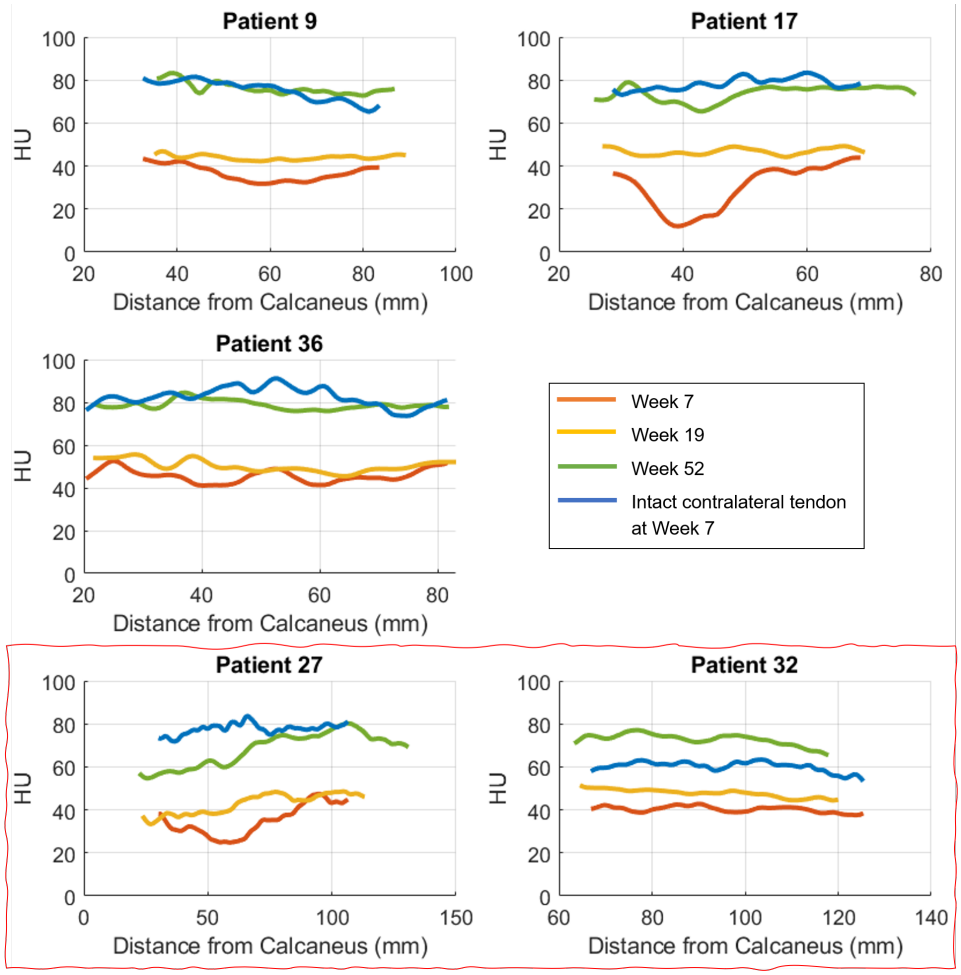

Figure 4.4: Tissue density measured in Hounsfield units from CT images taken at 7, 19 and 52 weeks post rupture of the segmented cross sections between the detected beads. For the CAT, the beads of the 7 week HAT was used to select an approximately equivalent section of the tendon. The results of the patients that are part of the test group are encircled.

Figure 4.5 show the mean intensity values of the radial sections that were split according to Figure 3.1. Overall, there is little change in mean intensities when separating the cross section radially. For some patients and time points, the outer section (continuous line) has lower mean intensities than the inner sections. The most variation between the radial sections appears in the 7 week scans for all patients. Some intensity variation patterns of Patient 27 remain throughout all time points of the HAT scans.

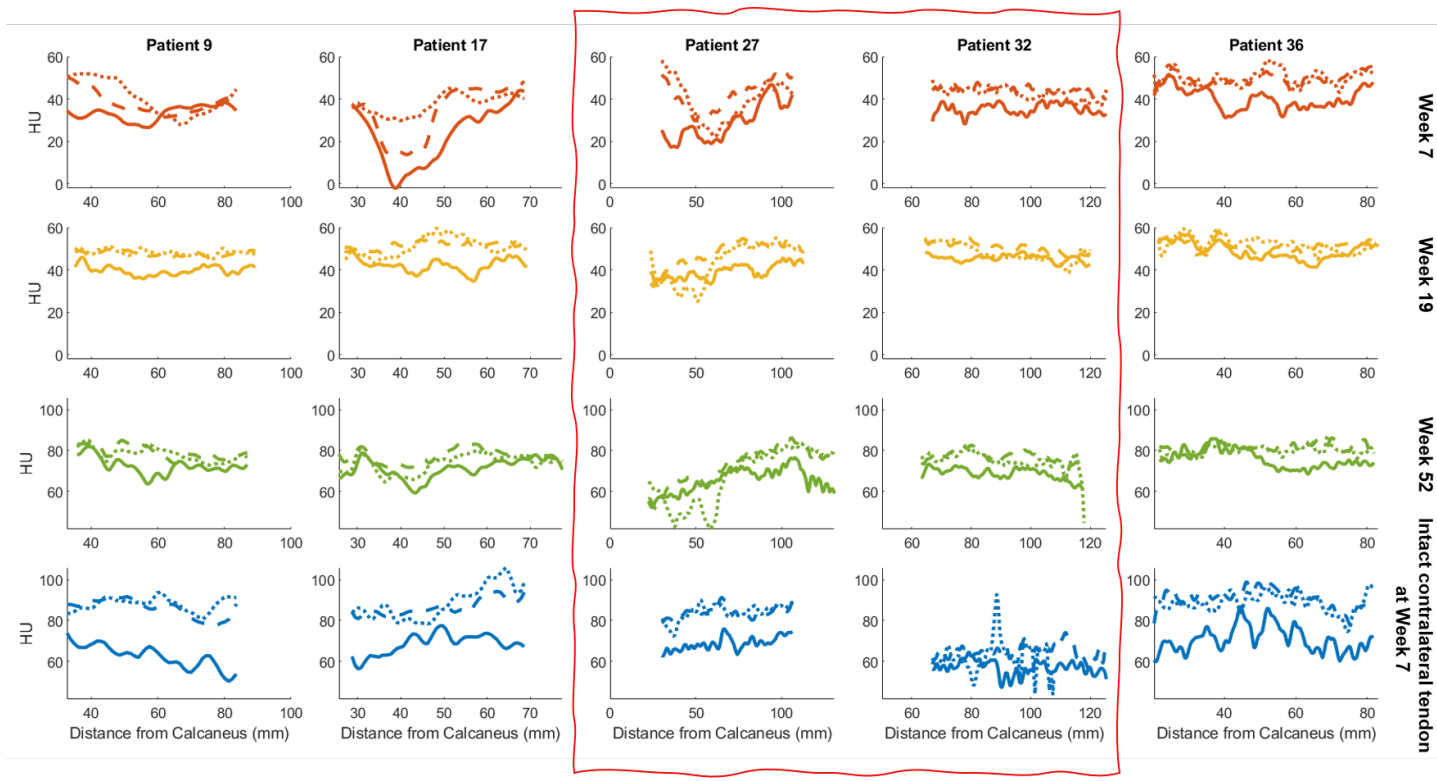

Figure 4.5: The tissue density measured in Hounsfield units from CT images taken at 7, 19 and 52 weeks post rupture of the segmented cross sections, separated in three radial sections. Only segmented tendon tissue between the beads were considered, or equivalent. The continuous line represents the outer section, the dashed line is the middle section and the dotted line corresponds to the innermost section. The results of the patients that are part of the test group are encircled.

4.2 Simulations

In this section the results from the simulation part of the project will be presented, beginning with the plots visualising the fitting of the stiffness parameters of the viscoelastic material. This is followed by stress and strain distribution plots from applying a 350 N load. For plots of stress and strain distributions from the application of 100 N, see Appendix A. Additionally, the displacement during the creep test for each time point (7, 19 and 52 weeks) is presented.

4.2.1 Fitting of stiffness parameters

The fitting of the stiffness parameters are presented together with the Young's modulus from the RSA data for each time point, Figure 4.6. The incline of the curves corresponding to the fitted parameters along with the Young's moduli of the RSA data are presented in Table 4.3. The fitted stiffness parameters are presented in Table 4.4 where the last row shows the degree of increase in stiffness parameters compared to the original rat model.

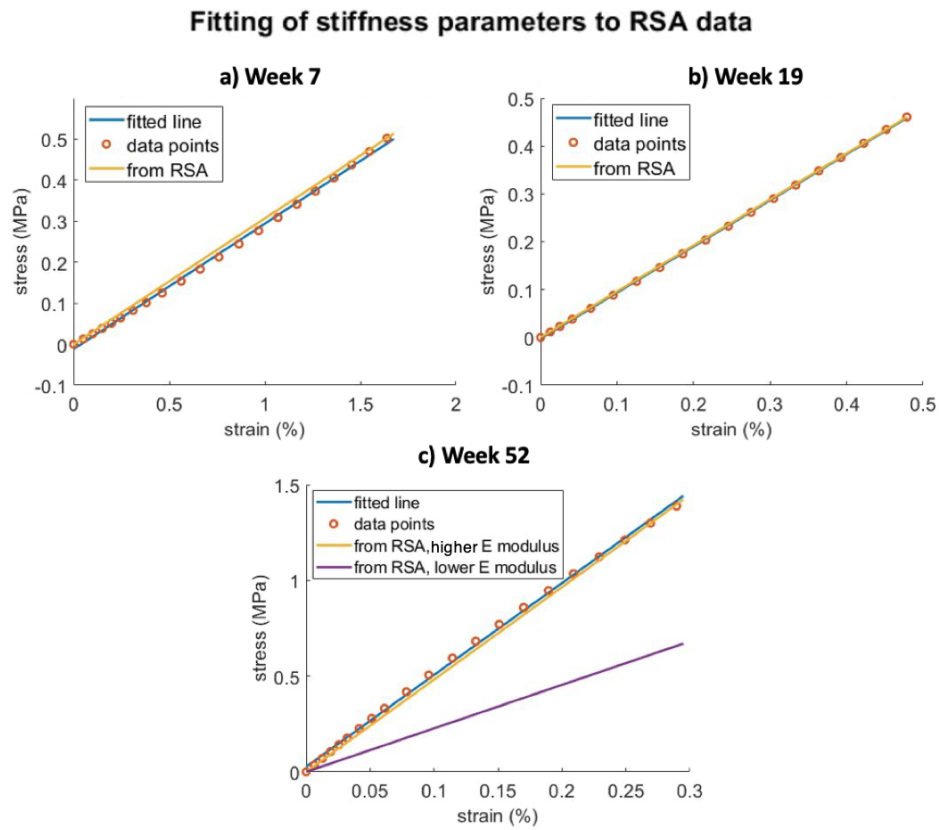

Figure 4.6: The result of the fitting of stiffness parameters, the incline of the yellow line represents the Young's modulus from the RSA data. The red circles are the data points from the simulation and the blue line is the linear approximation to the data points. The incline of this line is the Young's modulus of the fitted parameters. For week 52, two Young's modulus were provided in the RSA data, using a low load (225N; purple line) and a higher load (350N; yellow line). The fitting of the parameters for week 52 was only done for the higher load (the yellow line). The Young's modulus from the lower load (purple line) is plotted for comparison.

Table 4.3: The Young's modulus from the RSA data and the fitted incline of the stress-strain curve of the stiffness parameters of the viscoelastic material [27]. The error shows the difference between the experimental Young's modulus and the incline of the stress-strain curve obtained from the fitting of parameters.

	Week 7	Week 19	Week 52
Experimental Young's modulus (MPa)	30.68	96.12	482.4
Fitted Young's modulus (MPa)	30.59	96.32	479.7
Error (%)	0.29	0.21	0.56

Table 4.4: The original stiffness parameters (MPa) from the rat model [27] and the fitted stiffness parameters (MPa) at each time point for the subject-specific human model. E_1, K_1, E_2 and K_2 represent the collagen stiffness parameters and are modelled by the SLS seen in Figure 2.8, and E_p, E_n and G_{pn} are the transversely isotropic stiffness parameters [27].

	Original parameters	Fitted parameters		
	Rat model	**Week 7**	**Week 19**	**Week 52**
E_1	5.734	10.9	25.2	79.7
E_2	0.2000	0.38	0.880	2.78
k_1	0.7826	1.49	3.44	10.9
k_2	18.16	34.5	79.9	252
E_p	0.5000	0.950	2.20	6.95
E_n	1.000	1.90	4.40	13.9
G_{pn}	0.2683	0.510	1.18	3.73
Factor of rat stiffness parameters	**x1**	**x1.9**	**x4.4**	**x13.9**

4.2.2 Stress distribution

One part of the results from the simulations was the stress distribution in the Achilles tendon, both on the surface and in the cross section in the area where the rupture is assumed to have occured. In Figure 4.7 it can be seen that the stress in general is the largest in the areas with the smallest cross section area, and also at the top and bottom where the boundary conditions have been applied. For week 7 (Figure 4.7, 1-3a)), a region with increased stress can also be seen at the middle of the tendon, where the rupture is assumed to have happened. From the cross sectional stress distribution it can be deducted that the stress is in general larger on the posterior side of the tendon, see Figure 4.7.

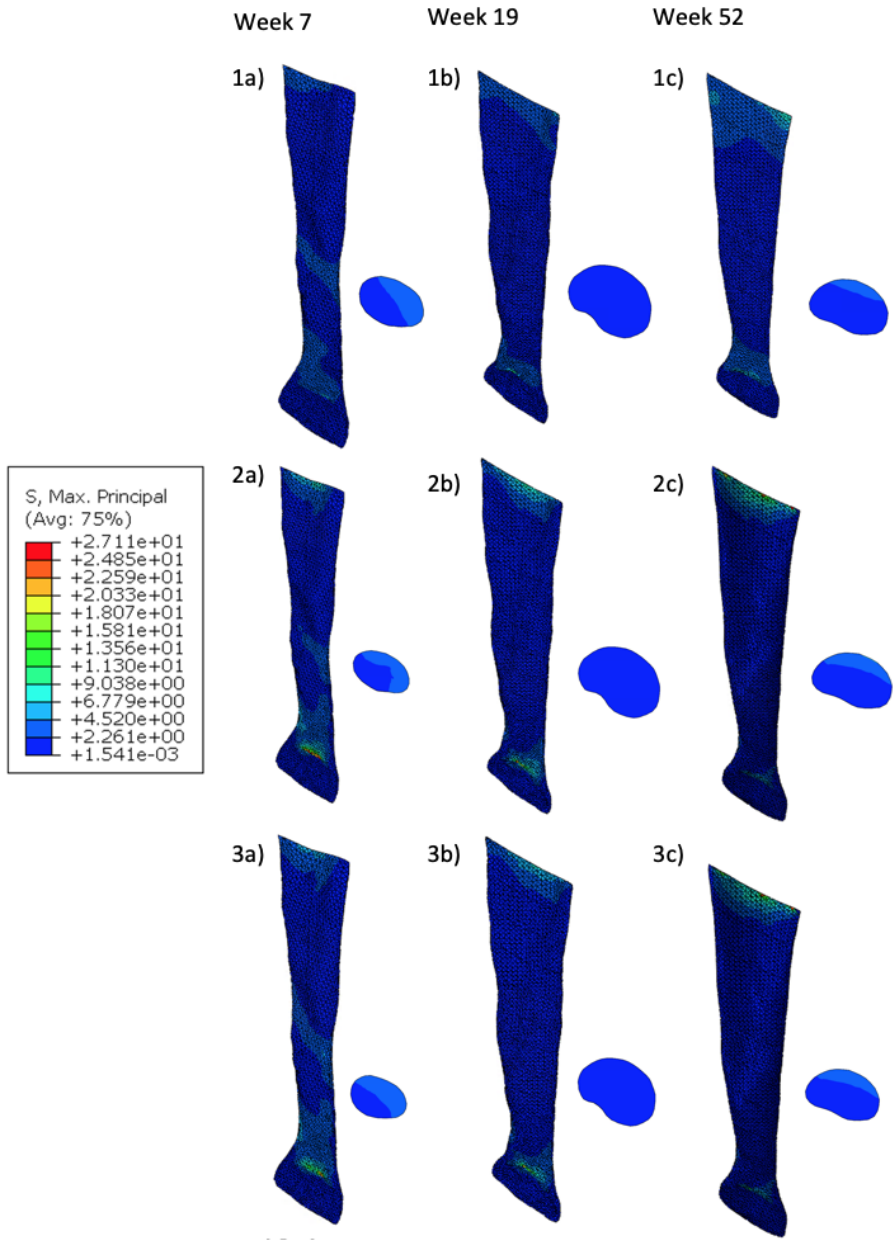

Figure 4.7: Stress distribution on the surface and in the cross section, approximately where the rupture is assumed to have occurred, at a 350 N load. 1a-c) show the stress distribution after the tensile test in the linear elastic material models at each time point. 2a-c) show the stress distribution of the tensile test of the viscoelastic material models for each time point. 3a-c) show the stress distribution at the end of the creep test of the viscoelastic material models for each time point. The stresses are in MPa.

4.2.3 Strain distribution

The strain in the tendon decreases during the healing process, see Figure 4.8. The greatest strain occurs in the HAT at week 7 at the end of the creep test, i.e. after 480 seconds (see Figure 4.8, 2a)). The maximum strain is located at the border corresponding to the calcaneal insertion, see Figure 4.8. For both week 7 and 19, the strain is largest in the areas with the smallest cross section, the same areas where the greatest stresses could be observed in Figure 4.7. The same applies to the cross section (Figure 4.8) where the greatest strain is located at the posterior side of the tendon. It is also clear that the week 7 HAT is the only tendon where the strain is apparent in the cross section at the assumed rupture point with an applied load of 350 N (Figure 4.8, 1-3a)).

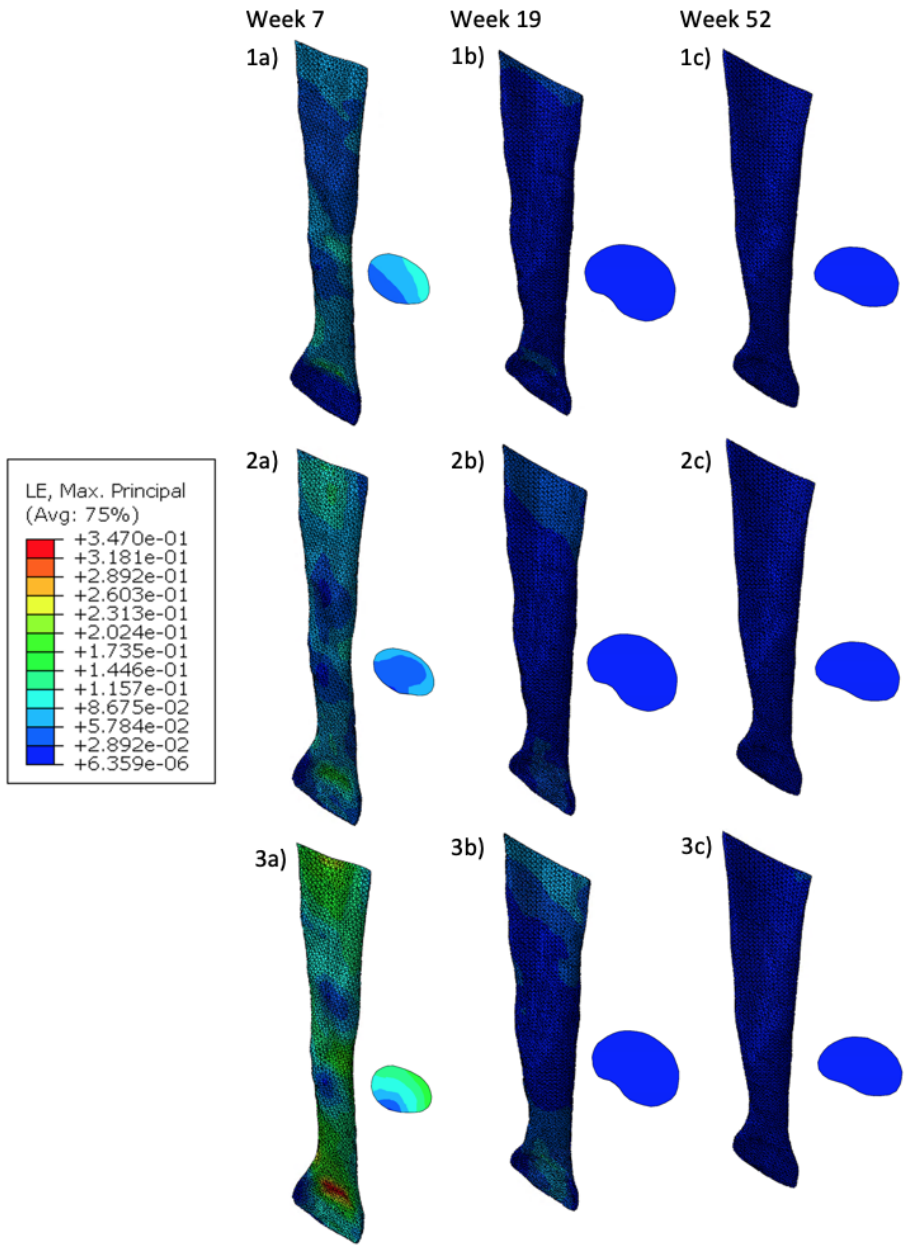

Figure 4.8: Strain distribution on the surface and in the cross section, approximately where the rupture is assumed to have occured, at a 350 N load. 1a-c) show the strain distribution after the tensile test in the linear elastic material models at each time point. 2a-c) show the strain distribution of the tensile test of the viscoelastic material models for each time point. 3a-c) show the strain distribution of the viscoelastic material models at the end of the creep test for each time point.

4.2.4 Creep test

The mean displacements of the top surface of the Achilles tendon was retrieved from the output of the simulation, these were plotted against time in order to visualise the displacement over time for each of the three time points (Figure 4.9).

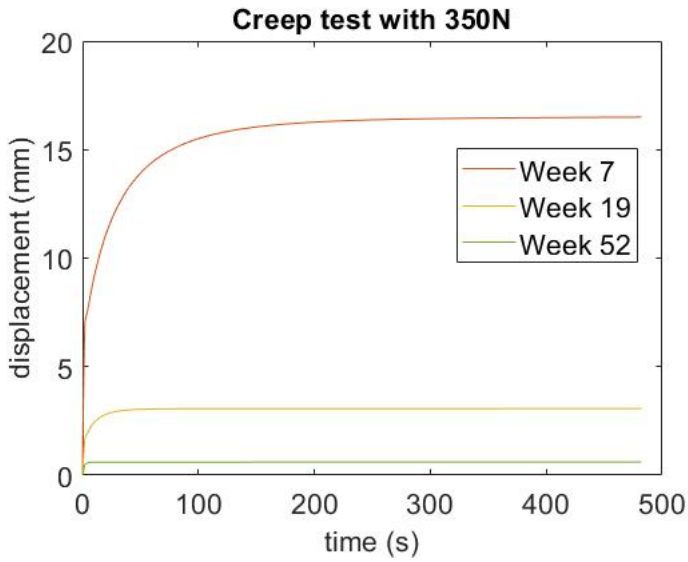

Figure 4.9: The figure shows the mean displacement of the nodes on the top surface of the subject-specific models, over the course of eight minutes when applying a constant load of 350 N, for the three time points.

Chapter 5

Discussion

In this section, a discussion regarding the image analysis results will be presented, followed by a discussion of the simulation results. Next, a joint discussion to connect the two main areas is presented. Lastly, a short comment on the ethics and a conclusion are presented.

5.1 Image analysis

An elongation of the Achilles tendon appear to have occurred some time prior to the 7 week check up. This is according to Table 4.1, with the assumption of the free tendon length being similar in both legs. This is true for healthy Achilles tendons [30]. The local minima found between the beads in the 7 week measurements of cross sectional area of the majority of the HATs (Figure 4.1), are likely indicating the location of rupture. Comparing the level of the ruptures located with the tendon length measurements of Table 4.1, it appears that the rupture occurred at or above the muscle-tendon junction. This is in agreement with literature [35], where the muscle-tendon junction is considered a weak part of the muscle-tendon unit. However, literature also states that the most common rupture site is at approximately 2 to 6 cm from the calcaneal insertion point, where the tendon cross sectional area is the smallest [42]. Hence, the rupture could have occurred distally to the muscle-tendon junction at the location of the smallest cross sectional area, and the tissue generated to bridge the tendon stumps was excessive. For all patients apart from Patient 36, the soleus does not appear as far distally as prior to rupture. The tendon elongation observed from time of rupture to the 7 week scan may have been caused by the formation of a new muscle-tendon junction

more proximal than before, as a consequence of rupture and regeneration of tissue. Alternatively, the tendon elongation observed may have been caused by the formation of new tendon tissue to bridge the gap between the two separated tendon stumps. Ultimately, with the data given, it is not possible to determine the cause of tendon elongation post rupture.

For all patients at the 19 week time point, there has been an increase in tendon callus cross sectional area compared to the 7 week time point, see Figure 4.1. This can be attributed to the regeneration of tissue, where there is a transition from the repairing phase to the remodeling phase at the 7 week time point [35] [40]. There is plenty of disorganised tissue and a high water content surrounding the rupture which is not identifiable as part of the tendon structure. This is also seen in Figure 4.4, where the mean Hounsfield units and tissue density is at its lowest between the implanted beads. At the 19 week time point, the tendon tissue is more organised and has turned scar like [35] [40], forming a callus around the rupture. The tissue density is slightly higher during this scan (Figure 4.4). After a year, Figure 4.1 shows that the cross section area has decreased again, but is at around twice the size as of the CAT. Comparing the tissue density between the healed tendon and the contralateral tendon presented in Figure 4.4, they appear similar overall. When observing the changes in tissue density radially from the centroid of the tendon in Figure 4.5, it can be noted that the outer section tends to be lower than the two inner sections. This is most likely due to the partial volume effect along with the segmentation selection, where some of the surrounding soft tissue has been included that has a higher water and/or fat content, bringing down the Hounsfield values. In turn, this observation implies that the results of Figure 4.4 are slightly underestimated. From this, it can be concluded that the tissue density between the beads has almost been restored to prior rupture levels, assuming healthy bilateral Achilles tendons prior rupture, but the cross sectional area is much larger than before.

The largest increase in tendon length between time of rupture and the 7 week check-up was seen in Patient 17, where the measured free tendon length has more than doubled, see Table 4.1. There is no change in the free length for Patient 36 as seen in the measurements. As both Patient 17 and Patient 36 are part of the control group, and the remaining three patients have measured elongation between 30-80%, no differentiating between the test group and the control group can be done here. Patient 27 and Patient 32 belong to the test group and from the results it appears they have the highest rupture points, considering the local minima of the week 7 plot in Figure 4.1 and the upper bead placement of Patient 32, whose rupture point is not apparent. The reason for the rupture point not showing for Patient 32 is perhaps due to a different rate of healing compared to the other patients. Patient 27

has a mineralisation in the distal part of the healing Achilles tendon, what effect this has is not know, however, this patient has low ATRS scores and have been unable to do heel raising according to Table 3.2. Patient 32 on the other hand consider the HAT to be fully functioning, although the heel raising score did not confirm this. An interesting observation regarding this patient is to look at the contralateral tendon, that shows some thickening distally in Figure 4.1 and has an overall lower tissue density than the healed tendon after 52 weeks. The cause of this is not known from this data, but could perhaps affect the self evaluating ATRS. With such a small sample size it is not possible to draw any conclusions, especially when the patients part of the test group present very different.

Both segmentation and measurement of the free tendon length have been performed manually, introducing user variability that has been limited by having the same person perform the task and in the case of determining the free tendon length. The measurement of tendon length is also dependent on voxel size and the plantar flexed angle of the ankle and foot, which for several patients varied between scans. This means that the top of the calcaneal tuberosity can vary between the time points and the varying tension in the viscoelastic tendon could potentially give different free tendon length, creating a variability to keep in mind.

5.2 Simulations

The human tendon is stiffer than the rat tendon, this can be seen in Table 4.4. The stiffness parameters increased consecutively with each of the three time points to better fit the subject-specific RSA data. This corresponds to the tendon getting stiffer as it heals. The material is viscoelastic and has both stiffness and dampening parameters. The experimental data provided by RSA methods represented tensile load, as the creep response is assumed to be negligible when the load has been applied for 10-15 seconds. In turn, it was only the stiffness parameters that could be adapted of the material properties. Consequently, the damping parameters were left untouched from the rat material model, which could potentially provide an unrealistic response in the human tendon model. The effects of the springs in the SLS are increasing in dominance compared to the dash pot as the stiffness is increased, resulting in that this effect will be most significant for week 52. As the dash pot is the element in the SLS that provides time dependency, which is characteristic for a viscoelastic material, this suggests that the tendon will behave more elastic. This is expressed in Figure 4.9, where the creep response is decreasing, showing less of a time dependency with each time point. This effect can

also be observed in Figure 4.8 where the strain distribution from the creep test progressively gets more like the strain distribution for the linear elastic model during the healing. In order to be able to fit all viscoelastic material parameters of the material model, more experimental data is needed. This could be achieved through a creep test for example.

In general, the stress and strain distribution are similar for the simulations of the tendon geometries with linear elastic properties and with the viscoelastic material properties for tensile testing (Figure 4.7 and 4.8). This result is suggesting what has been stated in literature regarding healthy Achilles tendons, where the tendon model geometry is more important than material properties when it comes to stress distribution changes [13]. This can in particular be seen in Figure 4.7, 1-2a), where the distribution is the most similar at week 7 for the linear material and the viscoelastic material at the end of the preloading step, representing tensile loading.

Both the stress and strain is the largest on the posterior side in the cross section at week 7 (Figure 4.7, 1-3a) and Figure 4.8, 1-3a)). This is suggesting that the geometry of the tendon needs to be straightened out during the deformation in such a way that the posterior side of the tendon is stretched slightly more. In Figure 4.7, 1-3c), this trend can also be observed for the 52 week time point for the stress. However, for the strain distribution in the cross sectional area this can only be observed for week 7 (Figure 4.8, 1-3a)). The cause of this is due to the high stiffness and the resulting low strains from the applied load. This effect appears to be caused by the geometry, which is given by the segmentation of the Achilles tendon from CT images. The relaxed tendon is gently curved towards the anterior, this is indicated in Figure 2.3, which is then straightened out when applying a tensile load.

The overall maximum strain observed is about 35 %, just above the fixed boundaries representing the calcaneal insertion at the end of the creep test for week 7 (Figure 4.8, 3a)). This can be considered to be boundary effects. However, there are experimental results from creep tests of human Achilles tendon from cadavers showing large strains of 20 % just above the calcaneal insertion [42]. The ATR occurred at the smallest cross sectional area of the tendon, where the observed strains were lower until just before failure [42]. In the area where the rupture is assumed to have occurred the maximum strain is about 17 % (Figure 4.8, 3a)) which is also very high considering a healthy Achilles tendon normally ruptures at about 11 % [41]. This suggests that in reality a creep test with 350 N for eight minutes is not suitable at 7 weeks post rupture. The patients at the 7 week time point were instead exposed to a lower load of 100 N, the simulation results of this load is presented in Appendix A. The maximum stresses for the two applied loads are between

6-28 MPa (Figure A1 and Figure 4.7), which is well below the limit where the tendon will rupture [41]. The strain is about 20 % just above the calcaneal insertion (Figure A2 in Appendix A) and about 7 % at the rupture site when applying a 100 N load. According to Wren *et al.* [41] a tendon will rupture at about 11 %, however according to another study by Wren *et al.* [42] the strain can be up to 20 % in the area above the calcaneal bone, this suggests that the tendon will not rupture when subjected to a load of 100 N at 7 weeks.

There are several limitations to these FE models of the human Achilles tendon. Firstly, the RSA data consists of isolated measurement results from tensile loading. The Young's modulus obtained from the subject-specific testing is derived from the assumption that the tendon is linear elastic between the beads. However, from the fitting plot in Figure 4.6c) for week 52 it is clear that two different loads generates two different Young's moduli, indicating that the linear approximation is not representative of the tendon behaviour. The loads used in the RSA study when experimentally determining the Young's modulus seems to include the toe region, with the exclusion of the higher stiffness modulus of week 52 (determined between the loads of 225 N and 350 N). The conclusion from this is that the fitting of the stiffness parameters is providing a material that is a very crude approximation of the actual tendon material. In addition, Figure 4.6c) also indicates that multiplying all stiffness parameters with the same factor is not ideal, as the material has the potential to mimic these types of changes in stiffness. A more realistic optimisation of parameters could have been achieved if more experimental data was available, with measurements at different loads.

Secondly, the applied boundary conditions are very simplified compared to reality. For example, the boundary conditions representing muscle contraction is applied at the top surface of the model, corresponding to the part of the tendon leading to the gastrocnemius muscles. Hence, the contraction of the soleus muscle is not contributing in this simplification, which similar to the setup of the creep testing of Achilles tendons from human cadavers performed by Wren *et al.* [42]. However, the applied boundary conditions in this project are still a closer representation of the *in vivo* Achilles tendon due to the advantage of being able to replicate calcaneal insertion compared to the clamping method in experiments by Wren *et al.* [42].

Thirdly, due to time constraints and insufficient number of experimental measurements no validation of the simulations was performed, this includes validating the mesh. If time had allowed, a validation could be done by comparing simulations of the same geometry with different mesh sizes to evaluate the eventual impact of the mesh. However, some trends have been

identified that corresponds to general data of healthy tendons, such as high strains above the calcaneal insertion [42].

5.3 Image analysis related to simulations

From the RSA data, the Young's moduli for the tendon tissue between the beads was provided. The geometry obtained from the CT images was of the entire tendon from the calcaenal insertion to the proximal end leading to the gastrocnemius muscles. The material properties given by the RSA data were assigned to the entire tendon. From what could be observed in Figures 4.1 and Figure 4.3, the entire tendon has thickened and generally has similar tissue density through out. A next step could be to look into density changes in more detail than what was done in this project in order to determine if a change in stiffness along and within the healing tendon can be discerned. This could then be applied to the FE model, providing more reality-based material changes within the tissue. Future FE models of the HAT could ultimately determine the failure force, and this knowledge could be used to prevent re-ruptures.

5.4 Ethics

The experimental data used in this project is from an ongoing unpublished study by Pernilla Eliasson. Written informed consent was obtained from all participants. Ethical approval was obtained from the Regional Ethical Review Board in Linköping (number 2014/69-31).

Using radiological methods to obtain geometry and loading effects in the tendon, the exposure to radiation must be considered. In particular if more measurements are needed to develop the model of healing human Achilles tendon, which was suggested. This may indicate the RSA method is not the optimal way to obtain these measurements.

For this master's thesis project, the data used came from other studies and thus was already existing. This meant that no additional exposure to radiation for the patients was required. The development of computational models can ultimately aid in better treatment options and allow *in silico* experiments, without the need for more patient data and *in vivo* experiments.

5.5 Conclusions

The free tendon length of the healing Achilles tendon increased prior to the 7 week scan, and overall did not change from then on. The cross sectional area of the healing tendon increased from 7 weeks to 19 weeks post rupture, and then decreased until 52 weeks post rupture. The tissue density slightly increased from 7 weeks to 19 weeks post rupture. At 52 weeks, the tissue density was overall returned to healthy tissue density. However, the cross sectional area had not returned to original thickness, indicating that none of the patients had fully recovered from ATR. No difference between the two patient groups given different treatments was discernible, mainly due to the small sample size and to the variability seen in patients.

Subject-specific FE models of the healing human Achilles tendon post rupture were created. The FE model had several limitations, including material properties determined from few experimental measurements that was taken around the rupture location. However, tissue density analysis showed that the density was not indicating variations of stiffness within the tendon. The simulations of the creep tests also showed similar results obtained from experimental results harvested human Achilles tendons, in particular highest strains observed in the tendon was near the calcaneal insertion.

Bibliography

[1] Element types. http://web.mit.edu/calculix_v2.7/CalculiX/ccx_2.7/doc/ccx/node32.html. Accessed: 2021-06-06.

[2] P. Aspenberg and T. Schepull. Substantial creep in healing human Achilles tendons. A pilot study. *Muscles Ligaments Tendons J*, 5(3): 151–155, 2015.

[3] S. Aufwerber, G. Edman, K. Grävare Silbernagel, and P. W. Ackermann. Changes in Tendon Elongation and Muscle Atrophy Over Time After Achilles Tendon Rupture Repair: A Prospective Cohort Study on the Effects of Early Functional Mobilization. *Am J Sports Med*, 48(13): 3296–3305, 11 2020.

[4] K. W. Barfod. Achilles tendon rupture; assessment of nonoperative treatment. *Dan Med J*, 61(4):B4837, Apr 2014.

[5] R. Bibb, D. Eggbeer, and A. Paterson. *Medical Modelling (Second Edition), pages 7-34*. Woodhead Publishing, Oxford, 2015.

[6] K. Bridwell and M. Rodts. Anatomical planes of the body. https://www.spineuniverse.com/anatomy/anatomical-planes-body. Accessed: 2021-06-06.

[7] CIBC, 2016. Seg3D: Volumetric Image Segmentation and Visualization. Scientific Computing and Imaging Institute (SCI). Version 2.2.1. Download from: http://www.seg3d.org.

[8] O. C. Dams, I. H. F. Reininga, J. L. Gielen, I. van den Akker-Scheek, and J. Zwerver. Imaging modalities in the diagnosis and monitoring of Achilles tendon ruptures: A systematic review. *Injury*, 48(11):2383–2399, Nov 2017.

[9] S. Demehri, M. Chalian, S. J. Farahani, E. K. Fishman, and L. M. Fayad. Detection and characterization of tendon abnormalities with

multidetector computed tomography. *J Comput Assist Tomogr*, 38(2): 299–307, 2014.

[10] M. N. Doral, M. Alam, M. Bozkurt, E. Turhan, O. A. Atay, G. Dönmez, and N. Maffulli. Functional anatomy of the Achilles tendon. *Knee Surg Sports Traumatol Arthrosc*, 18(5):638–643, May 2010.

[11] P. Eliasson, A. S. Agergaard, C. Couppé, R. Svensson, R. Hoeffner, S. Warming, N. Warming, C. Holm, M. H. Jensen, M. Krogsgaard, M. Kjaer, and S. P. Magnusson. The Ruptured Achilles Tendon Elongates for 6 Months After Surgical Repair Regardless of Early or Late Weightbearing in Combination With Ankle Mobilization: A Randomized Clinical Trial. *Am J Sports Med*, 46(10):2492–2502, 08 2018.

[12] G. G. Handsfield, J. M. Inouye, L. C. Slane, D. G. Thelen, G. W. Miller, and S. S. Blemker. A 3D model of the Achilles tendon to determine the mechanisms underlying nonuniform tendon displacements. *J Biomech*, 51:17–25, 01 2017.

[13] W. Hansen, V. B. Shim, S. Obst, D. G. Lloyd, R. Newsham-West, and R. S. Barrett. Achilles tendon stress is more sensitive to subject-specific geometry than subject-specific material properties: A finite element analysis. *J Biomech*, 56:26–31, 05 2017.

[14] T. T. Huttunen, P. Kannus, C. Rolf, L. Felländer-Tsai, and V. M. Mattila. Acute achilles tendon ruptures: incidence of injury and surgery in Sweden between 2001 and 2012. *Am J Sports Med*, 42(10):2419–2423, Oct 2014.

[15] C. A. HyperWorks. *Hypermesh*. Altair Engineering, Inc., Troy MI, United States, 2021.

[16] A. Inc. Meshmixer 3.5. `http://www.meshmixer.com/`. Accessed: 2021-03-11.

[17] W. Kalender. *Computed tomography : fundamentals, system technology, image quality, applications*. 2000.

[18] H. Khayyeri, G. Longo, A. Gustafsson, and H. Isaksson. Comparison of structural anisotropic soft tissue models for simulating Achilles tendon tensile behaviour. *J Mech Behav Biomed Mater*, 61:431–443, 08 2016.

[19] R. Korhonen and S. Saarakkala. *Biomechanics and Modeling of Skeletal Soft Tissues*. 11 2011.

[20] G. A. Lichtwark, A. G. Cresswell, and R. J. Newsham-West. Effects of running on human Achilles tendon length-tension properties in the free and gastrocnemius components. *J Exp Biol*, 216(Pt 23):4388–4394, Dec 2013.

[21] Lumen. Anatomical orientation and directions. `https://courses.lumenlearning.com/ap1x94x1/chapter/anatomical-orientation-and-directions/`. Accessed: 2021-06-06.

[22] Z. Ma, J. M. Tavares, R. N. Jorge, and T. Mascarenhas. A review of algorithms for medical image segmentation and their applications to the female pelvic cavity. *Comput Methods Biomech Biomed Engin*, 13(2): 235–246, 2010.

[23] N. Maffulli. The clinical diagnosis of subcutaneous tear of the Achilles tendon. A prospective study in 174 patients. *Am J Sports Med*, 26(2): 266–270, 1998.

[24] MATLAB. *9.8.0.1538580 (R2020a)*. The MathWorks Inc., Natick, Massachusetts, United States, 2020.

[25] MATLAB and I. P. Toolbox. *9.8.0.1538580 (R2020a)*. The MathWorks Inc., Natick, Massachusetts, United States, 2020.

[26] K. Nilsson-Helander, R. Thomeé, K. G. Silbernagel, K. Grävare-Silbernagel, P. Thomeé, E. Faxén, B. I. Eriksson, and J. Karlsson. The Achilles tendon Total Rupture Score (ATRS): development and validation. *Am J Sports Med*, 35(3):421–426, Mar 2007.

[27] T. Notermans, H. Khayyeri, and H. Isaksson. Understanding how reduced loading affects Achilles tendon mechanical properties using a fibre-reinforced poro-visco-hyper-elastic model. *J Mech Behav Biomed Mater*, 96:301–309, 08 2019.

[28] N. Ottosen and H. Petersson. *Introduction to the Finite Element Method, pages 1-6*. Prentice Hall, Harlow, England, 1992.

[29] S. H. Park, H. S. Lee, K. W. Young, and S. G. Seo. Treatment of Acute Achilles Tendon Rupture. *Clin Orthop Surg*, 12(1):1–8, Mar 2020.

[30] N. N. Patel and S. A. Labib. The Achilles Tendon in Healthy Subjects: An Anthropometric and Ultrasound Mapping Study. *J Foot Ankle Surg*, 57(2):285–288, 2018.

[31] T. Schepull and P. Aspenberg. Early controlled tension improves the material properties of healing human achilles tendons after ruptures: a randomized trial. *Am J Sports Med*, 41(11):2550–2557, Nov 2013.

[32] T. Schepull and P. Aspenberg. Healing of human Achilles tendon ruptures: radiodensity reflects mechanical properties. *Knee Surg Sports Traumatol Arthrosc*, 23(3):884–889, Mar 2015.

[33] T. Schepull, J. Kvist, C. Andersson, and P. Aspenberg. Mechanical properties during healing of Achilles tendon ruptures to predict final outcome: a pilot Roentgen stereophotogrammetric analysis in 10 patients. *BMC Musculoskelet Disord*, 8:116, Nov 2007.

[34] J. Schindelin, I. Arganda-Carreras, E. Frise, V. Kaynig, M. Longair, T. Pietzsch, S. Preibisch, C. Rueden, S. Saalfeld, B. Schmid, J. Y. Tinevez, D. J. White, V. Hartenstein, K. Eliceiri, P. Tomancak, and A. Cardona. Fiji: an open-source platform for biological-image analysis. *Nat Methods*, 9(7):676–682, Jun 2012.

[35] P. Sharma and N. Maffulli. Biology of tendon injury: healing, modeling and remodeling. *J Musculoskelet Neuronal Interact*, 6(2):181–190, 2006.

[36] V. B. Shim, J. W. Fernandez, P. B. Gamage, C. Regnery, D. W. Smith, B. S. Gardiner, D. G. Lloyd, and T. F. Besier. Subject-specific finite element analysis to characterize the influence of geometry and material properties in Achilles tendon rupture. *J Biomech*, 47(15):3598–3604, Nov 2014.

[37] V. B. Shim, G. G. Handsfield, J. W. Fernandez, D. G. Lloyd, and T. F. Besier. Combining in silico and in vitro experiments to characterize the role of fascicle twist in the Achilles tendon. *Sci Rep*, 8(1):13856, 09 2018.

[38] D. Systèmes. Abaqus/cae 2020. `https://www.3ds.com/products-services/simulia/products/abaqus/`. Accessed: 2021-06-06.

[39] D. Systèmes. *SolidWorks*. Dassault Systèmes SOLIDWORKS Corp., Waltham, Massachusetts, USA, 2020.

[40] J. H. Wang. Mechanobiology of tendon. *J Biomech*, 39(9):1563–1582, 2006.

[41] T. A. Wren, S. A. Yerby, G. S. Beaupré, and D. R. Carter. Mechanical properties of the human achilles tendon. *Clin Biomech (Bristol, Avon)*, 16(3):245–251, Mar 2001.

[42] T. A. Wren, D. P. Lindsey, G. S. Beaupré, and D. R. Carter. Effects of creep and cyclic loading on the mechanical properties and failure of human Achilles tendons. *Ann Biomed Eng*, 31(6):710–717, Jun 2003.

Appendix A

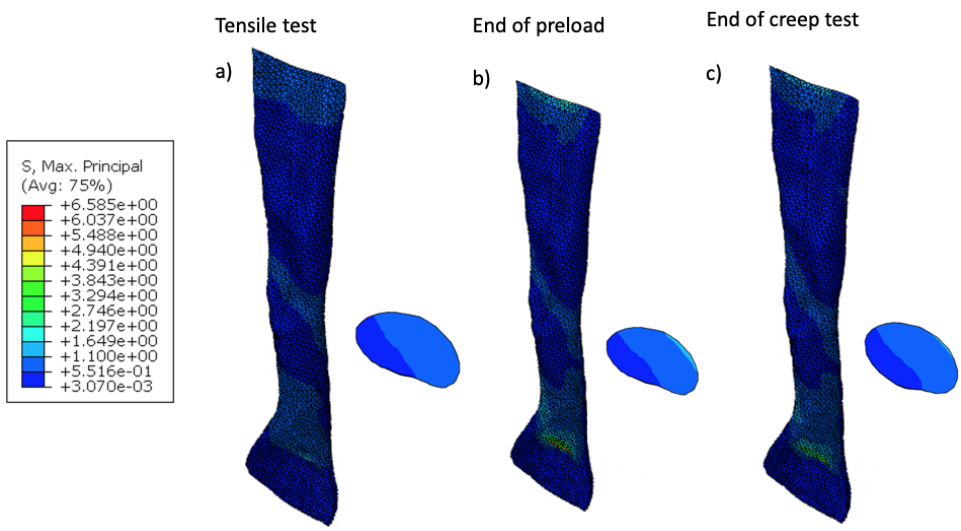

Figure A1: The stress distribution on the surface and in the cross section, approximately where the rupture is assumed to have occured, for the tendon 7 weeks post rupture. The tests were performed with a 100 N load. The stresses are in MPa. For the tensile test the linear elastic material was used, for the preload and creep the user defined vicoelastic material was used.

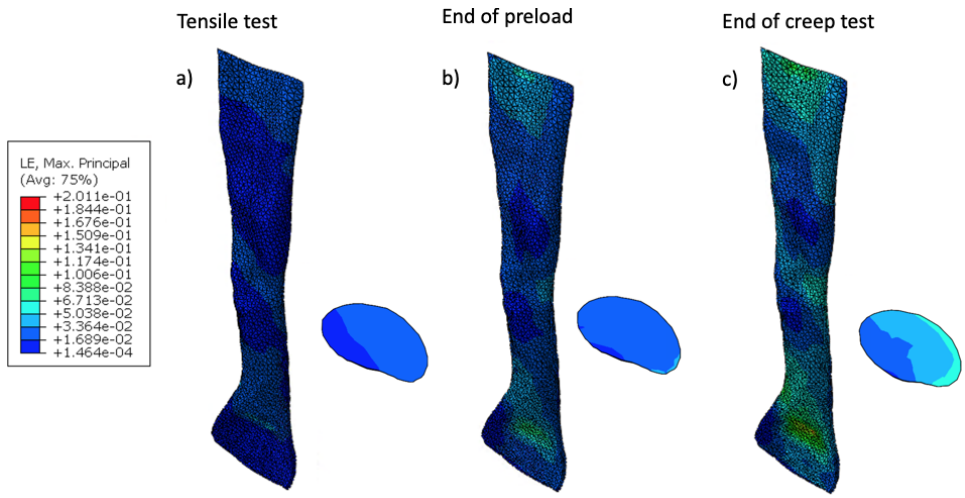

Figure A2: The strain distribution on the surface and in the cross section, approximately where the rupture is assumed to have occured, for the tendon 7 weeks post rupture. The tests were performed with a 100 N load. For the tensile test the linear elastic material was used, for the preload and creep the user defined vicoelastic material was used.